

*CONDUCTIVE AND PHOTOCONDUCTIVE AFM ON EXFOLIATED MoS<sub>2</sub>*

AS  
36  
2019  
PHYS  
.L44

A Thesis submitted to the faculty of  
San Francisco State University  
In partial fulfillment of  
the requirements for  
the Degree

Master of Science

In

Physics

by

Hao Lee

San Francisco, California

May 2019

Copyright by  
Hao Lee  
2019

CERTIFICATION OF APPROVAL

I certify that I have read CONDUCTIVE AND PHOTOCONDUCTIVE AFM ON EXFOLIATED MoS<sub>2</sub> by Hao Lee, and that in my opinion this work meets the criteria for approving a thesis submitted in partial fulfillment of the requirement for the degree: Master of Science in Physics at San Francisco State University.



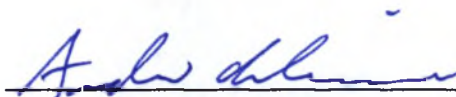
---

AKM Newaz Ph.D.  
Professor of Physics



---

Huizhong Xu Ph.D.  
Professor of Physics



---

Andrew S Ichimura Ph.D.  
Professor of Chemistry

## *CONDUCTIVE AND PHOTOCONDUCTIVE AFM ON EXFOLIATED MoS<sub>2</sub>*

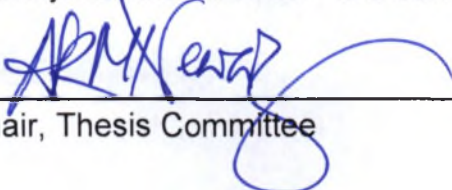
Hao Lee  
San Francisco State University  
2019

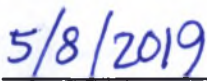
Transition metal dichalcogenides (TMDs) are layered semiconducting van der Waal crystals and promising materials for a wide range of electronic and optoelectronic devices. Realizing practical electrical and optoelectrical device applications of MoS<sub>2</sub> requires a metal junction. Hence, a complete understanding of electronic band alignments and the Schottky barrier heights governing the transport through TMD-metal junction is critical. However, it is unclear how energy band of different TMD layer aligns while in contact with a metal. In pursuit of removing this knowledge gap, we have studied conducting atomic force microscopy (CAFM) of atomically thin layered MoS<sub>2</sub> (1-5 layers) immobilized on atomically flat conducting Au surfaces (RMS surface roughness <0.2 nm) and indium tin oxide (ITO) substrate (RMS surface roughness <0.7 nm) forming a vertical metal (conductive-tip)-semiconductor-metal device. We have observed that the current increases as the number of layers increases up to 5. By applying Fowler-Nordheim tunneling theory, we have determined the barrier heights for different layers and observed that the barrier height decreases as the number of layers increases. Using density functional theory (DFT) calculation, we successfully demonstrated that the electron affinity (barrier height) increases

(decreases) as the layer number increases. By illuminating the TMDs on a transparent ultra-flat conducting ITO substrate, we observed a reduction in current when compared to the current measured in the dark, hence demonstrating negative photoconductivity. Using the lock-in technique, we are able to separate the DC current due to the constant applied voltage from the photocurrent (oscillating with modulation frequency  $\sim 9.8$  kHz) due to the illumination. We illuminated the samples using a laser (480 nm) with various intensities/voltage bias and observed the photocurrent responses of the samples under different conditions.

Our study provides a fundamental understanding of the local electronic and optoelectronic behaviors of TMD-metal junction that are dependent on layer numbers and may pave the way toward developing nanoscale electronic devices with tailored properties of different layers.

I certify that the Abstract is a correct representation of the content of this thesis.

  
\_\_\_\_\_  
Chair, Thesis Committee

  
\_\_\_\_\_  
Date

## ACKNOWLEDGEMENTS

I would like to thank Dr Newaz for giving helpful guidance for this research and providing necessary materials and equipment for the experiments. Also Miss Diana in facility CMIC has been helpful in training me on how to use the Atomic Force Microscopy and solving other technical issues I may have encountered while operating the instrument. Dr Ishimura's group helped produce the evaporated gold substrates that we relied heavily on and are critical for our experiments. My appreciation also goes to other collaborators who are not mentioned but contributed to this study. Without these helps, it would have been more difficult to make progress in this study.

## TABLE OF CONTENTS

1 Introduction .....	1
1.1 Metal-semiconductor contact (Schottky junction).....	3
1.2 Band diagram of MoS <sub>2</sub> .....	4
1.3 Barrier height .....	5
1.4 Electrical properties .....	7
1.5 Optical properties.....	8
2 Experimental method .....	10
2.1 Procedures .....	10
2.2 Mechanical exfoliation.....	15
2.3 Conductive-atomic force microscopy (C-AFM) .....	17
2.4 Ramen microscopy .....	18
3 Electrical properties of the MoS <sub>2</sub> .....	20
3.1 ITO and TS-Au (Template stripped Au) substrates.....	22
3.2 Barrier height measurements.....	23
3.3 Barrier height dependence on substrates .....	25
3.4 Density functional theory (DFT) .....	28
4 Optical properties of MoS <sub>2</sub> .....	31
4.1 Negative conductance under illumination .....	32
4.2 Photocurrent measurements using lock-in amplifier .....	34
4.3 Dependence of photocurrent on layer number.....	35
4.4 Photothermoelectric effect (PTE).....	39
5 Conclusion.....	41
Appendix .....	43
References .....	45

## LIST OF FIGURES

Figure	Page
1.1 A small piece of thin MoS <sub>2</sub> sheet held on a tweezer.....	2
1.2 Left: The atomic structure of the MoS <sub>2</sub> crystal in one unit cell. Right: The top view of the MoS <sub>2</sub> crystal structure .....	2
1.3 Schematically drawing of the structure of a transition metal dichalcogenide (TMD) crystal, MoS <sub>2</sub> (not to scale) sitting on top of a glass slide (ITO) coated with a thin layer of gold (~20 – 50 nm). .....	4
1.4 The bandgap of the MoS <sub>2</sub> depends on the number of layers .....	5
1.5 Left: The Schottky junction forms when a metal is in contact with a semi-conductor. Right: The energy band diagram of the metal-semiconductor contact .....	6
1.6 Four different current transport processes between a metal-semiconductor contact .....	7
2.1 Laminar fume hood used for sample preparation .....	11
2.2 ITO glass wafer with a conductive coating on one side .....	11
2.3 Left: An ITO glass with exfoliated MoS <sub>2</sub> flakes on the conductive side. Right: A 50x optical image of MoS <sub>2</sub> flakes .....	11

2.4	An schematic drawing of our AFM setup .....	12
2.5	Left: Optical image of the acoustical noise isolation box. Right: The lockin amplifier and a frequency filter connected to the AFM electrical panel.....	13
2.6	The AFM head and the Zeiss optical microscope. ....	14
2.7	Left: Optical image of a 4 inches diameter Si wafer coated with ~50 nm thick Au for making template stripped substrates. Right: A template stripped Au substrate glued on top of an ITO glass substrate .....	15
2.8	Left: A piece of clean template stripped Au substrate. Right: The optical image of a mechanically exfoliated MoS <sub>2</sub> crystal on blue tape prior to transferring to the gold coated substrate .....	15
2.9	Left: the height profile of a MoS <sub>2</sub> crystal measured by the contact mode AFM. Right: The current profile of the sample .....	18
2.10	Raman spectroscopy measures the peak separation for each layer .....	19
3.1	MoS <sub>2</sub> sample on a template-stripped Au substrate.....	21
3.2	Layer dependent conductive AFM measurement of MoS <sub>2</sub> sample on a template-stripped Au substrate .....	23
3.3	Layer dependent conductive AFM measurement of MoS <sub>2</sub> sample on a physical vapor deposited ITO film. ....	27

3.4	DFT calculated interfacial electronic structure of the Au/MoS <sub>2</sub> .....	29
4.1	An external light source (460-490 nm) provides an illumination to the MoS <sub>2</sub> sample from the bottom of the C-AFM stage .....	31
4.2	Photoconductive AFM measurement of sample on an ultra-flat ITO coated single crystal quartz .....	33
4.3	A schematic drawing of the photocurrent measurements setup .....	34
4.4	The sample MoS <sub>2</sub> nano-sheet sample used for photocurrent study .....	35
4.5	A C-AFM current image showing photocurrent response of MoS <sub>2</sub> .....	36
4.6	The photocurrent (AC) of MoS <sub>2</sub> measured with voltage going from 0V to 1V while keeping the laser intensity constant (maximum power) .....	37
4.7	The photocurrent (AC) of MoS <sub>2</sub> measured with the laser intensity going from small to large while keeping the applied voltage constant .....	38
4.8	Normalized photoresponse for the first few layers of MoS <sub>2</sub> .....	38
4.9	The PTE effect was seen when the sample was applied with zero voltage and was shone with the light.....	40
A1	Surface roughness of thermally evaporated Au substrate, template-stripped Au substrate and commercially available ITO on glass substrate.....	43
A2	current map of MoS <sub>2</sub> sample on an ITO substrate .....	44

A3 Calculated work function of MoS<sub>2</sub> on Au as a function of the thickness of MoS<sub>2</sub> and the interfacial spacing between the first layer of MoS<sub>2</sub> and the Au (111) surface ..... 44

## Chapter 1

### Introduction

Transition metal dichalcogenides (TMDs) with the formula,  $MX_2$ , where M is a transition metal element from group IVA (Ti, Hf), group VA (V, Nb or Ta) or group VIA (W, Mo) and X is a chalcogen (S, Se or Te) belong to a group of layered materials that form a prismatic trigonal unit cell of the X-M-X form, where a transition metal atom separates two hexagonal planes of the chalcogen atoms [1, 2]. The crystal  $MoS_2$  is one of the most abundant TMD layered materials in nature. The optical image of a naturally grown  $MoS_2$  flake is shown in Fig 1.1. TMDs are van der Waals crystal and provide the tantalizing prospect of miniaturizing semiconductor devices to truly atomic scales and accelerating the advances of many two-dimensional (2D) optoelectronic devices [3-8]. These atom thick layered TMDs (Fig 1.2) demonstrate some unique properties that include 2D confinement, direct band-gap nature [1], varying band structure with layer thickness [1, 9, 10], and weak screening of charge carriers enhancing the light-matter interactions [1, 9, 11]. High photon absorption ( $\alpha \sim 10\%$  for visible light and  $\alpha \sim 40\%$  for ultraviolet photons) [1, 12], and exciton formation (a hydrogenic entity made of an  $e-h$  pair) [1, 12] make TMDs very attractive for different optoelectronic applications [3, 13-17] including sensitive photodetectors [13, 18-20], energy harvesting devices [21-23], monolayer light emitting diodes (LEDs) [14, 16, 17], single photon sources [24-28], and nanocavity lasers [29].



Figure 1.1 - A small piece of thin MoS<sub>2</sub> sheet held on a tweezer. A 0.1 cm thick MoS<sub>2</sub> sheet contains roughly over 1.5 million number of layers. A monolayer of MoS<sub>2</sub> is three atoms thick and consists of two hexagonal planes of atoms (sulfur) with a hexagonal plane of metal atoms (Molybdenum) sandwiched in between. This kind of monolayer structure is known as Transition metal dichalcogenide (TMD). The structure of a TMD is shown in Fig 1.2.

Fig 1.2 (left) is the 3-D atomic structure of the MoS<sub>2</sub> in which S and Mo atoms bonded together in a triangular prismatic fashion. Fig 1.2 (right) is the top view of the structure. The thickness of each TMD layer is around 0.65 nm and each layer is bonded together by the weak van der Waals force. Fermi level and the density of state depends on how the layers are stacked together.

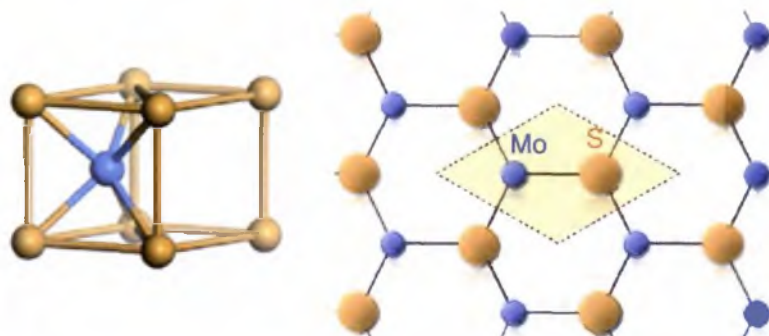


Figure 1.2 – Left: The atomic structure of the MoS<sub>2</sub> crystal in one unit cell. The middle layer consists of Molybdenum atoms sandwiched by two layers made of sulfur atoms. Right: The top view of the MoS<sub>2</sub> crystal structure [30].

## 1.1 Metal-semiconductor contact (Schottky junction)

When a semiconductor is in contact (Schottky junction) with a metal (Fig 1.3) the band structure of the semiconductor is modified. Electronic and optoelectronic devices require such metal-semiconductor junctions for current injection and collection. Interfacial charge transport properties play a critical role in governing the current injection or collection in a metal-semiconductor junction. One property that controls charge transport across the junction is the barrier height due to the conduction band offset between the TMD and metal. Although significant progress has been made in demonstrating many different types of TMD-based devices, it is not clear how the barrier heights change with TMD thickness at the few layers level (1L-5L) [10]. One standard technique to elucidate the barrier height is through the measurement of the electron affinity by ultraviolet photoelectron spectroscopy (UPS). However, UPS requires a large sample size that is challenging to prepare by exfoliation of MoS<sub>2</sub>.

One possible alternative experimental route employs scanning probe microscopy (SPM) to study local electrical transport and optoelectronic properties of few-layer TMDs. Since these 2D TMDs materials conform to the surface roughness of the substrate, SPM requires that the sample resides on a surface with sub-nanometer roughness (root mean square (RMS) surface roughness < 1 nm). To understand the dependence of the barrier height on TMD layer thickness, we performed conductive atomic force microscopy (CAFM) and photocurrent atomic force

microscopy (PCAFM) of few-layer  $\text{MoS}_2$  samples immobilized on ultra-flat transparent indium tin oxide (ITO) and template-stripped Au conducting surfaces.

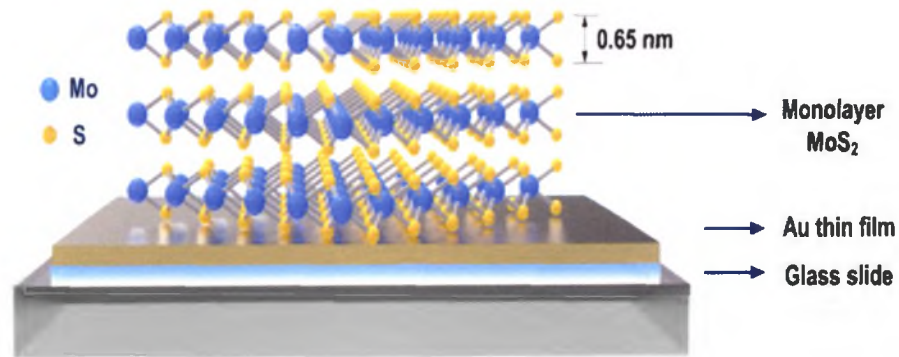


Figure 1.3 – Schematic drawing of the structure of a transition metal dichalcogenide (TMD) crystal,  $\text{MoS}_2$  (not to scale) sitting on top of a glass slide (ITO) coated with a thin layer of gold (~20 – 50 nm). The thickness of each  $\text{MoS}_2$  layer is about 0.65 nm and each layer is bonded together by the weak van der Waals force [31]. The interface between the  $\text{MoS}_2$  crystal and the substrate forms a Schottky junction.

## 1.2 Band diagram of $\text{MoS}_2$

Energy band diagrams (Fig 1.4) show the energy levels of the electrons in the material. This energy gap reflects the amount of energy that would be needed to remove an electron from its parent atom. The energy difference between the conduction band and the valence band commonly referred as the band gap sets the required transition energy for electrons and holes. When the thickness of the material is reduced down to a few layers, the properties of the material will change due to the quantum confinement effect. The band-gap decreases with an increase in the number of layers. Single layer  $\text{MoS}_2$  has a direct band-gap (~1.8 eV) at K-point in Brillouin zone [32]. In the case of a direct band-gap semiconductor, a

photon can generate electron-hole pairs without requiring a phonon marking the semiconductor optically active. The direct band-gap nature of monolayer MoS<sub>2</sub> enables many applications in optoelectronics, ranging from ultrasensitive photodetectors to nano-laser [33].

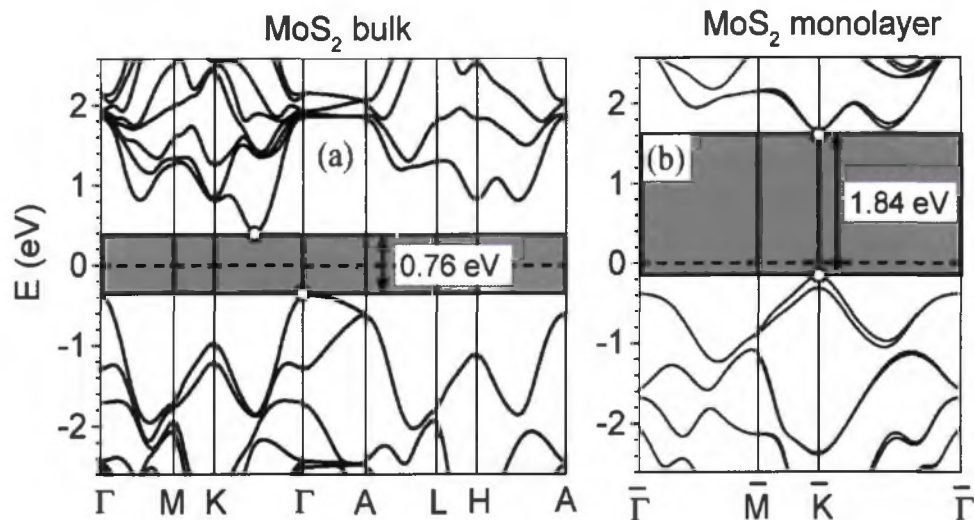


Figure 1.4 – The energy band diagram of MoS<sub>2</sub> depends on the number of layers [29]. The band-gap decreases as the number of layers increases. The band-gap transitions from indirect to direct as the MoS<sub>2</sub> goes from bulk to monolayer. The direct band-gap of the monolayer is calculated to be about 1.8 eV.

### 1.3 Barrier height

The barrier height (Schottky barrier height), also denoted by  $\phi_B$ , is the energy barrier between the metal and semiconductor when in contact. This barrier height determines the current transporting between a metal-semiconductor contact. These metal-semiconductor contacts are used as the gate electrodes of a field-effect transistor, MESFETs (metal–semiconductor field-effect transistor) and photodetectors and solar cells [34].

When a metal is in contact with a semiconductor, the Fermi level of the semiconductor will line up with the Fermi level of the metal by exchanging the electrons. When a potential is applied between the metal and the semiconductor, the charge will flow from one material to another in order to reach thermal equilibrium. When a forward bias voltage is applied, the Fermi-level in the semiconductor is lower than the Fermi level in the metal by an amount equal to the difference between the two workfunctions [35]. The workfunction ( $W$ ), is the energy required to bring an electron from the Fermi level of the material to the vacuum level. This workfunction is related to the barrier height by the following Eq (1.1).

$$\phi_B = W - \chi_e \quad (1.1)$$

where  $\chi_e$  is the electron affinity of the metal and  $W$  is the work function of the metal as shown in Fig 1.5. In our experiment, we measured the barrier height in a MoS<sub>2</sub>-metal contacts and compared it with the theoretical values.

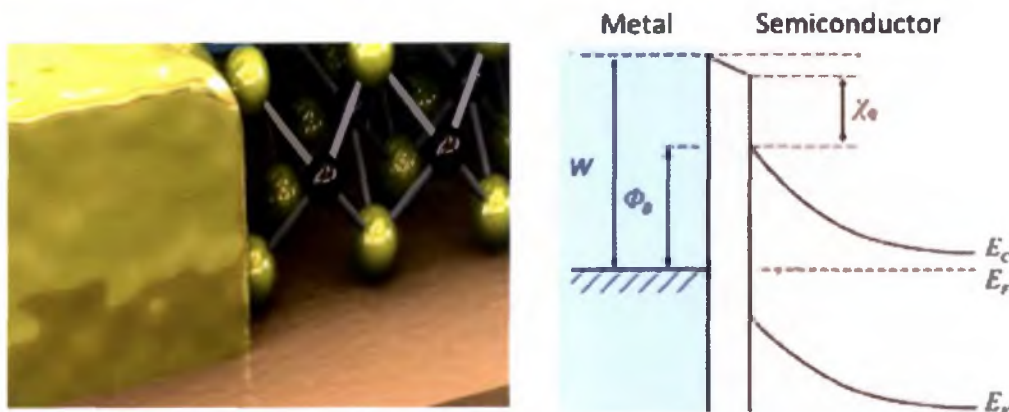


Figure 1.5 – Left: The Schottky junction forms when a metal is in contact with a semiconductor [20]. Right: The energy band diagram of the metal-semiconductor contact [36] where  $\chi_e$  is the electron affinity depending on the type of the materials, work function  $W$  is the energy required to bring the electron from the Fermi level to the vacuum level, and barrier height  $\phi_B$  is the difference of these two parameters.

## 1.4 Electrical properties

The current transport between the metal-semiconductor contacts due to the majority carriers has four basic mechanisms (Fig 1.6) .

These four mechanisms are (a) transport of electrons from the semiconductor over the potential barrier into the metal; (b) quantum-mechanical tunneling of the electrons through the barrier; (c) recombination in the space-charge region (d); and, hole injection from the metal to the semiconductor.

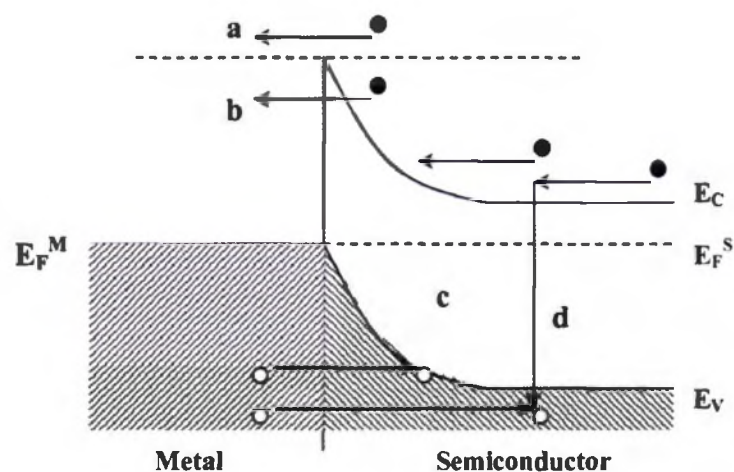


Figure 1.6 – Four different current transport processes between a metal-semiconductor contact [37]. The black dots in the diagram represent the free carriers which flow in one direction.

In our experiment, we relied on the second current transport mechanism (b) to extract the barrier height information of the materials. This is because the equation from the Fowler Nordheim model we used to calculate the barrier height works under the forward bias in which the electrons pass through barrier potential by tunneling effect. There are a few different methods to measure the barrier height based on the first current transport mechanism. They are current-voltage

measurement [35], activation energy measurement [35], capacitance-voltage measurement [35], and photoelectric measurement [35]. In our experiment, we study the barrier height using the current-voltage measurement to extract the  $I$ - $V$  characteristics of the device in the forward bias regime. After obtaining the  $I$ - $V$  characteristics, we then used the Fowler-Nordheim (FN) model to calculate the barrier height [38]. For our experiment, we studied the barrier height dependence on the layer thickness, the type of the substrate and other experimental conditions.

### 1.5 Optical properties

Light-matter interaction for  $h\nu > E_g$  in a semiconductor creates an electron-hole ( $e$ - $h$ ) pair with electrons in the conduction band and holes in the valence band. This creates free carriers and essentially produces an observable photocurrent in the samples illuminated by photons with energy higher than the band-gap. The increase in electrical conductivity due to the photo-generated  $e$ - $h$  pairs is called photoconductivity. Without illumination, the conductivity is given by Eq (1.2).

$$\sigma_0 = e \cdot (n_0\mu_e + p_0\mu_h) \quad (1.2)$$

Where  $n_0$  and  $p_0$  are the electron and hole concentrations at equilibrium, respectively, and  $\mu_e$ ,  $\mu_h$  are the electron and hole mobilities, respectively.

When the light is on, the free carriers, electrons, and holes are created in pairs and so the number of the electrons and holes are increased by the same amount  $\Delta n$  and  $\Delta p$ . The new conductivity with the light is then given by Eq (1.3)

$$\sigma = \sigma_0 + e \cdot \Delta n (\mu_e + \mu_h) \quad (1.3)$$

where  $\Delta n = \Delta p$

Similar to the electrical properties, photo-generated carriers also depend on the number of layers and other parameters, such as frequency and intensity of the incidence light. These carriers are continually created by the incident beam and the excess carriers are continually annihilated by recombining with each other. In the later chapter, we will explore the relation of the photoconductivity with the thickness of the MoS<sub>2</sub> materials.

To probe the layer dependence of interfacial transport properties, CAFM and PCAFM measurements of few-layer MoS<sub>2</sub> samples with thickness varying from monolayer (1L-MoS<sub>2</sub>) to 5 layers (5L-MoS<sub>2</sub>) were performed. To understand the effect of the tip on the electrical and optical properties, Pt/Ir tips and platinum silicide (Pt/Si) tips were used for both CAFM and PCAFM measurements. Similar results were observed for both Pt/Ir tips and Pt-Silicide (Pt/Si) tips. Here we present the results obtained using Pt/Si tips unless mentioned otherwise. We have studied three MoS<sub>2</sub> samples on Au substrate and three MoS<sub>2</sub> samples on ITO coated substrate. All samples behaved similarly with respect to their electronic and optoelectronic properties.

## Chapter 2

### Experimental method

#### 2.1 Procedures

Layered materials or van der Waals crystals do not have out-of-plane bonding to the neighboring layers, which interact through weak van der Waals forces. That is why one can easily remove layers from the bulk crystal using a minuscule force. Using this property, it is possible to isolate monolayer nanosheet using a preformed polymer tape (e.g. Scotch tape by 3M™) also known as mechanical exfoliation or micro-exfoliation. Prof. Geim and Prof. Novoselov first successfully applied this technique to isolate graphene, monolayer graphite, in 2004 [39].

The size and the shape of the remaining flakes on the tapes might be random, however, the flakes obtained this way preserves the natural properties of the material. In other exfoliation methods, such as chemical or laser exfoliation, the properties of the samples could be altered during the process and that will significantly affect the outcome of the measurements.

A single crystal layered MoS<sub>2</sub> was mechanically diced into small pieces in a shape of sheets. The thin MoS<sub>2</sub> sheet was then further exfoliated using scotch tapes repeatedly. The remaining MoS<sub>2</sub> crystal on the tapes will eventually reach an atomic thickness consisting of only a few layers after several times of exfoliation. The tape was placed gently on top of the desired substrate and scratched on the

upper side with a tweezer. This exfoliation process was done inside a laminar fume hood (Fig 2.1) to reduce the risk of the adsorption of contaminants onto the sample.



Figure 2.1 – A photograph of the laminar fume hood used for sample preparation. A high efficiency particulate air (HEPA) filter was used to produce a clean space.



Figure 2.2 – Left: A photograph of the ITO glass wafer (4 inches diameter) with a conductive ITO coating on one side.



Figure 2.3 – Left: A photograph of an ITO coated glass with exfoliated MoS<sub>2</sub> flakes. Right: Optical image of the flakes in 50x magnification.

The conductive ITO-coated glass wafer (Fig 2.2) was diced into smaller pieces (Fig 2.3 left) followed by cleaning using acetone and isopropanol. We mechanically exfoliated MoS<sub>2</sub> on the ITO coated side of the glass wafer.

The surface roughness on this conductive side is around 0.65 nm in Root Mean Square (RMS). We examined the exfoliated MoS<sub>2</sub> nano-sheet using an optical microscope with high magnification (20x and 50x). One optical micrograph of the exfoliated sample is shown in Fig 2.3 (right). We also conducted Raman spectroscopy measurement to confirm the sample type.

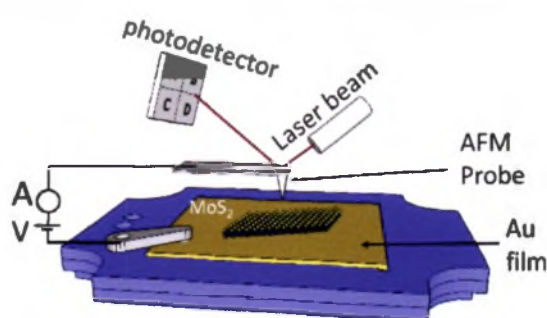


Figure 2.4 – An schematic drawing of our AFM setup. The laser reads the bending of the probe-tip to reconstruct the surface image of the sample (MoS<sub>2</sub>).

Once a potential flake is identified, we placed the sample on the C-AFM (Fig 2.4) for further tests. Initially, we used Pt/Ir tips manufactured by Applied-nano Inc. The metal coating on the tips is necessary for the conductive measurements. We applied a bias voltage between the ITO substrate and the probe to measure the current. The voltage is applied to the metal substrate. The current was amplified by a preamplifier (gain  $\sim 10^8$  A/V). We simultaneously measured the height and current profiles along the surface of the flake. The resolution of a typical data matrix is usually set to be 256 x 256 pixels.

To analyze the data, we used the JPK software provided by the AFM manufacturer and open-source software, Gwyddion [40]. For customized and sophisticated data analysis, we wrote our own program using Python language.

To reduce the acoustical noise, the AFM system is placed inside an isolation cage as shown in (Fig 2.5 left). The C-AFM unit is mounted on an inverted Zeiss optical microscope (Fig 2.6). To illuminate the sample, an external light source (X-Cite 110 LED) is connected to this microscope through a liquid waveguide. The intensity of the LED light source is also tunable allowing us to perform intensity dependent property measurements. The fluorescent filters inside the microscope allow us to select the wavelength of the light illuminating the sample. There are three fluorescent filters available in our system ( $690\pm 30$  nm,  $540\pm 20$  nm,  $610\pm 30$  nm). To obtain the clean photocurrent, we superposed the TTL (Transistor-Transistor Logic) signal generated by the lock-in amplifier with our light source under a modulation frequency ( $\sim 9.8$  KHz). The TTL pulse acts as a step-function signal and controls the on-and-off of the light. Therefore only the photocurrent superposed with the modulation frequency will be detected from the output channels (Fig 2.5 right).



Figure 2.5 – Left: Optical image of the acoustical noise isolation box. Computers on the left control the AFM and the Zeiss inverted microscope inside the chamber. Right: The lock-in amplifier and a frequency filter are connected to the AFM electrical panel. This helps distinguish photocurrent (AC current) from the DC current in the output channels.

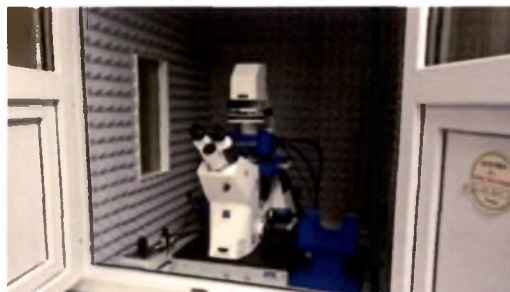


Figure 2.6 -The actual AFM head and the Zeiss optical microscope. The external light illuminating the sample is guided by a microscope objective (40x) with a numerical aperture of 0.75.

To reduce ambient light pollutions and acoustic noise, measurements were conducted with closed leads and in a dark environment. The average temperature inside the chamber is around 22 °C. The temperature can vary by a few degrees over the duration of our measurements. To elucidate the local nanoscale optoelectronic properties of our sample, we conducted photocurrent scan of the sample under different illuminations in this controlled environment. For the best outcome of the experiments, we always used fresh new AFM cantilever probes.

Since atomic thick 2D materials conform to the surface roughness, it is critical for us to study samples on substrates that are also atomically flat. Since the thickness of the monolayer-MoS<sub>2</sub> is only ~0.7 nm, the surface roughness of the substrate should be less than the thickness of the monolayer. Commercially available conductive substrates are usually designed for photovoltaic devices and have a high surface RMS roughness (> 10nm). Hence, we have prepared conducting substrate which has surface roughness comparable to the thickness of a monolayer MoS<sub>2</sub> crystal (RMS roughness <1 nm). We will now discuss in details all the experimental techniques used in this research.

## 2.2 Mechanical exfoliation



Figure 2.7 – Left: Optical image of a 4-inch diameter Si wafer coated with ~150 nm thick Au for making template stripped substrates. Right: A piece of ITO glass coated with a 150 nm thick Au after applying the template stripping technique. Since the skin depth of Au is in the visible spectrum ~20nm, these samples are partially transparent.

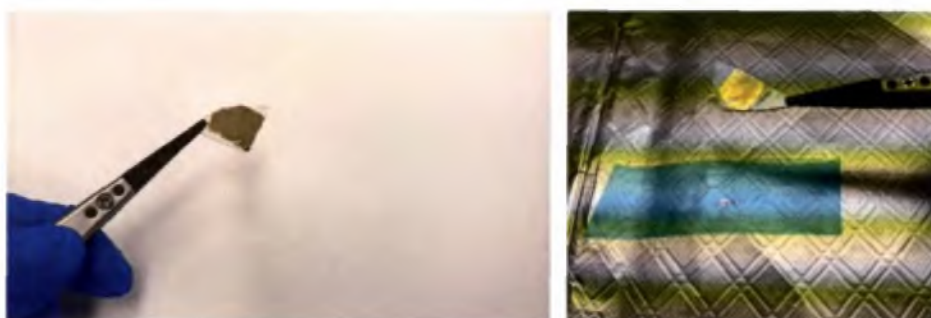


Figure 2.8 – Left: A piece of clean template stripped Au substrate. Right: The optical image of a mechanically exfoliated MoS<sub>2</sub> crystal on blue tape prior to transferring to the gold-coated substrate. The MoS<sub>2</sub> on the blue tape is transferred onto the clean substrate in less than five minutes, which reduces the contamination on the substrate surface due to exposure to ambient air.

After the flakes were separated from exfoliation, the next step is to transfer them from the tapes onto a substrate (Fig 2.8). Many experimental factors involved in this transfer process that seem trivial but could totally change the yield of the good samples such as, the type of the tapes, the pressure applied when the tape is placed on the substrate, temperature, air quality, and the time duration in which the exfoliated flakes on the tape is in contact with the substrate before being peeled off. The cleanness of the substrate surface is also critical. It takes many trials and errors to optimize the sample fabrication procedures.

The substrates also play an important role in obtaining good samples. The commercially available ITO coated glass substrates have an acceptable conductivity values, but the surface roughness ranges from a few nano meters to tens of nano meters. This high surface roughness creates challenges to conduct precision electrical and electro-optical measurements.

To obtain atom thick MoS<sub>2</sub> crystal on an ultra-flat transparent substrate, we prepared indium tin oxide (ITO) thin films using physical vapor deposition technique onto transparent Z-cut quartz substrates. The films were sputtered from an as-purchased ITO target in a 10 mTorr Ar ambient at 65 W DC plasma deposition power at room temperature, with a deposition rate  $\approx$  3 nm/min. Multiple film thicknesses were tried and the corresponding change in film properties with and without a 400 °C vacuum anneal was evaluated. In this work, we have employed a 20-nm-thick ITO film, which has a surface roughness  $\sim$ 0.7 nm. The substrate was prepared at Stanford University in collaboration with Prof. Eric Pop's group.

In this research, we have also studied electrical transport properties on a non-transparent Au substrate prepared by template stripped techniques (Fig 2.7 left). We have prepared a thick Au film ( $\sim$ 150 nm) on a wafer by using the thermal evaporator in a UHV environment (pressure $\sim$ 10<sup>-8</sup> Torr). Next, we attached the wafer coated with the thin Au film with the diced ultra-flat silicon wafer (1 cm  $\times$  1 cm) by using a water-resistant potting compound (Devcon 2-Ton<sup>®</sup> Epoxy). To dry the epoxy and make a strong attachment, the diced wafer/epoxy/deposited-Au-film

pieces were kept under pressure created by a block of heavy metal (5~7 pounds) for 24 hours. Finally, the diced pieces were peeled using a blade and the thin Au film that remained on the ultra-flat silicon wafer makes the surface of the silicon wafer even flatter. The RMS roughness of this template stripped Au surface is about ~0.2 nm. To avoid any organic contamination of the freshly peeled Au surface, we micro-exfoliated the MoS<sub>2</sub> flakes within ~ 5 minutes after peeling off.

Besides the substrates, surface residues from the tapes or the chemicals used during the exfoliation can also affect the quality of the samples greatly. Since the samples are stored in ambient condition, it can adsorb unwanted particles. That is why we always cleaned the sample by flushing with acetone and isopropanol before the measurement.

### 2.3 Conductive-atomic force microscopy (C-AFM)

The C-AFM relies on the conductive coating on the probes/tips to measure the current (Fig 2.9). In theory, the AFM is able to resolve the images down to a few nanometers, but in the actual experiment, the maximum resolution of the images is limited by several other experimental factors. The most common one is the size and shape of the cantilevers used to probe the samples. A brand-new CAFM cantilever tip used in this study has a sharpness of about 20 nm in diameter but this sharpness wears out after some measurement scans and the width of the tip-front becomes wider. We observed that our Pt/Silicide cantilever tips normally wear after 20-30 full scans. Therefore, we used a fresh cantilever tip for each new measurement session to obtain consistent data.

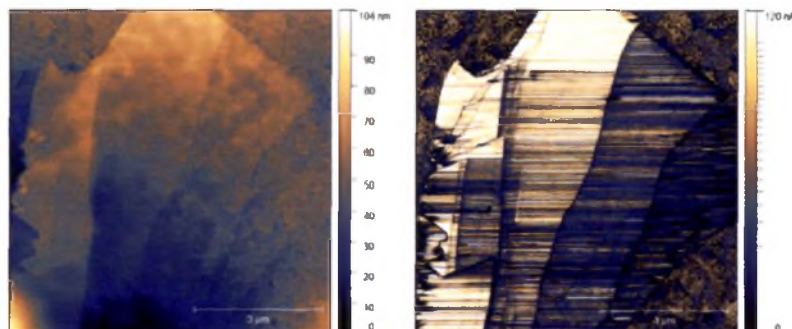


Figure 2.9 – Left: the height profile of a MoS<sub>2</sub> crystal measured by the contact mode AFM. Right: The current profile of the sample measure simultaneously. The imaging area is 7.5×7.5 μm<sup>2</sup> and the image size is 512 pixels × 512 pixels.

We have used two types of conducting tips, Pt/Ir tips ( Model: ANSCM-PC, Coating: Platinum, W: 40 μm, L: 450 μm, T: 2.5 μm, Resonance Frequency: 5-25 kHz, Force Constact: 0.02-0.8 N/m) from applied Nanotsrcures Inc. and Pt-Si tips (Model: PtSi-CONT, Coating: Sicilide, W: 50 μm, L:450 μm, T: 2 μm, Resonance Frequency: 6-21 kHz, Force Constact: 0.02-0.77 N/m) from Nanoandmore company. We have found that Pt/Si tips are more robust and give more consistent data than the Pt/Ir tips.

## 2.4 Raman spectroscopy

Raman spectrometry is one of the most important optical analytical research tools in physics, chemistry and engineering disciplines. Raman spectra provides the vibrational fingerprints of the chemical bonds within molecules or atomic lattices in a given pure substance or a complex material, allowing the reliable identification of chemical species and are thus used heavily in identifying different 2D layered materials. There are two types of vibrational modes in MoS<sub>2</sub> (as in all layered structures): vibrational modes inside layers (intralayer) and modes resulting from

the movements of complete layers (interlayer). The intralayer modes are primarily related to the chemical composition of a layer (or layers) and are their fingerprint. We have used our micro-PL setup to study the Raman spectroscopy. The samples were illuminated by a 532 nm green laser and the Raman signal was analyzed by a high resolution spectrometer using 1800 lines/mm grating. The light was collected by a thermoelectrically cooled CCD camera. The Raman spectra obtained for one of our samples is similar to the plots shown in Fig 2.10. The two peaks appearing at  $\sim 385 \text{ cm}^{-1}$  and  $408 \text{ cm}^{-1}$  are the characteristic Raman signature of the intralayer vibrations of bulk MoS<sub>2</sub> crystal. The peak separation shows the difference between the excitation wavelength ( $E_{2g}$ ) and the wavelength ( $A_{1g}$ ) after the Raman scattering. The amount of the the shift in wavelength after scattering depends on the vibrational rotational and bending forces within chemical bonds of molecule.

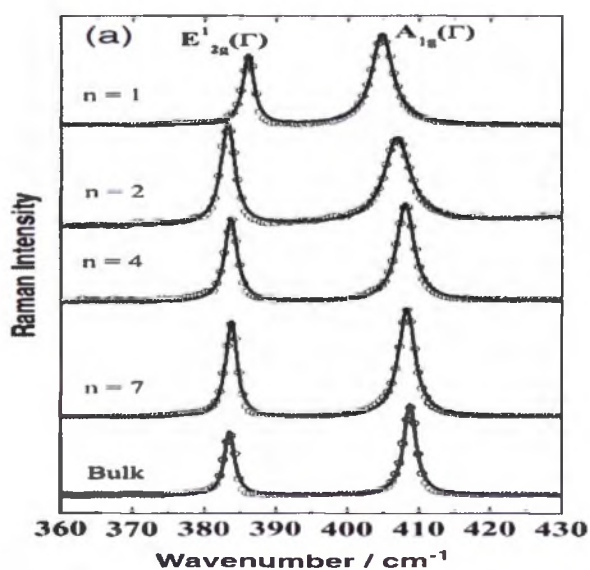


Figure 2.10 – Raman spectroscopy measures the peak separation in terms of wavenumber for each MoS<sub>2</sub> layer [41].

## Chapter 3

### Electrical properties of MoS<sub>2</sub>

#### 3.1 ITO and TS-Au (Template-stripped Au) substrates

Figures 3.1(a) and 3.1(b) show an optical image and the corresponding contact mode AFM height profile image of exfoliated MoS<sub>2</sub> on a freshly peeled template-stripped (TS) Au surface. Template-stripped Au substrate was prepared following standard procedures [42-45] (see Methods for details). The 1L-5L layer MoS<sub>2</sub> sheet structure is clearly observed in the contact mode AFM height profile image, Fig. 3.1(b). Before carrying out CAFM and PCAFM measurements, the RMS roughness of the TS-Au and ITO substrates were measured and found to be 0.2 nm and 0.7 nm, respectively.

The ultra-smooth nature of the TS-Au surface is very close to the surface roughness of hexagonal boron nitrides (*h*-BN) [46], a layered material commonly used as an atomically flat substrate. For comparison, the RMS roughness of the external surface of the thermally evaporated (TE) gold layer was 2 nm. The left and right insets to Fig.3.1(c) show tapping mode height profile images of the TS-Au and ITO coated surfaces, respectively (see Appendix information Fig.A1 for an AFM image of a TE coated AU surface). Fig.3.1(c) also compares the height histograms of the TS and TE gold surfaces confirming that template stripping produces a uniformly smooth surface with a narrow full-width-half-maximum

(FWHM) distribution while the distribution and roughness of the TE surface are an order of magnitude larger. We have found that employing an ultra-flat conducting surface as a substrate for exfoliated TMD is critical to observe consistent electrical and optoelectronic properties of atomically thin MoS<sub>2</sub> crystals.

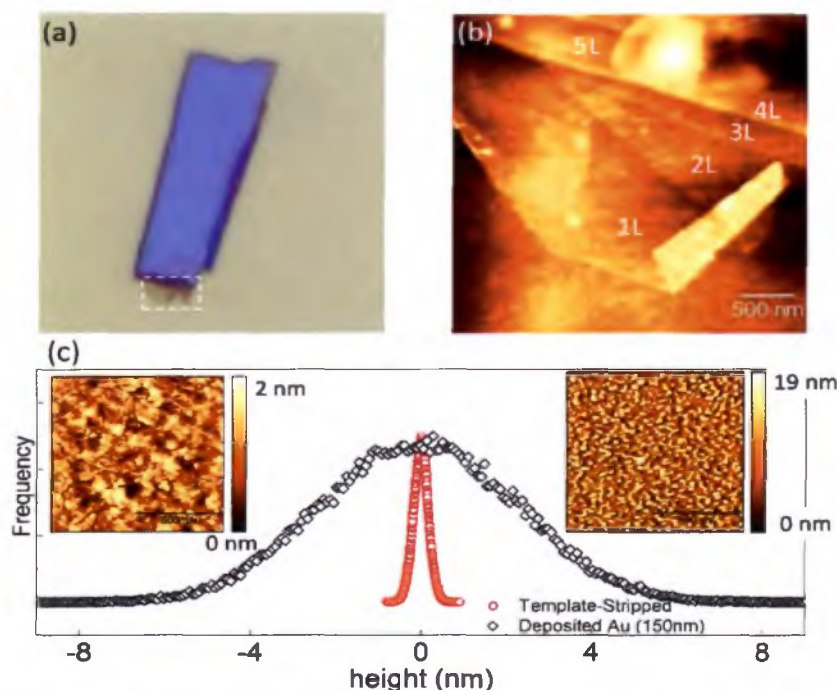


Figure 3.1 - MoS<sub>2</sub> sample on a template-stripped Au substrate. (a) Optical image of a MoS<sub>2</sub> sample. The dotted square region is studied using AFM and CAFM. (b) The height profile AFM image of the marked area (white dotted-square) in Fig. (a) measured by AFM contact mode. Region of different layer number is shown. The scale bar is 500 nm. (c) Histogram of the height distribution (surface roughness measured by AFM) of the template-stripped Au substrate and as deposited Au substrate of thickness  $\sim 150$  nm. The Au for the template stripping was deposited on a single crystal Si wafer. The root mean squared (RMS) value of the surface roughness measured was  $\sim 0.18$  nm for template-stripped Au and  $\sim 1.8$  nm for as deposited substrate. Inset-left: tapping mode AFM image of the template-stripped Au surface. Inset-right: tapping mode AFM image of an as deposited Au substrate on Si wafer. The area of the scanned region is  $1 \mu\text{m} \times 1 \mu\text{m}$ . The scale bar is 500 nm. A Gaussian fit to the height data provides full width at half maxima (FWHM)  $\sim 0.3$  nm for the template-stripped Au and  $\sim 5$  nm for as deposited Au. The surface roughness profile of template-stripped Au is very similar to surface roughness observed for *h*-BN (see text).

### 3.2 Barrier height measurements

Now we discuss the electronic transport behavior of the MoS<sub>2</sub> sample on template-stripped Au substrate. Fig. 3.2(a) shows schematically the experimental setup used to measure the current under an applied voltage. The bottom inset shows the configuration of the sample with respect to the SiO<sub>2</sub>/Si substrate. The MoS<sub>2</sub> sample was directly micro-exfoliated onto the TS-Au surface. Fig. 3.2(b) presents the DC current map measured with a 0.4 V bias of the sample whose height profile is shown in Fig. 3.1(b). The spatial current map clearly demonstrates that the current increases as the layer number increases. This feature becomes clearer in the *I-V* curves obtained by averaging over a specific layer number as shown in Fig. 3.2(c). Almost zero current was observed for the Au substrate outside the MoS<sub>2</sub> flake (Fig. 3.1(b)). We attribute the non-conducting behavior observed for the gold substrate to two factors, the small force constant ( $\sim 0.2$  N/m) of the cantilever and the adhesive residue from the tapes used for the exfoliation created a thin insulating film on the surface of the substrate blocking the tip/substrate contact. The force constant of the tip was too small to scratch the surface contaminants to make direct contact to the Au surface.

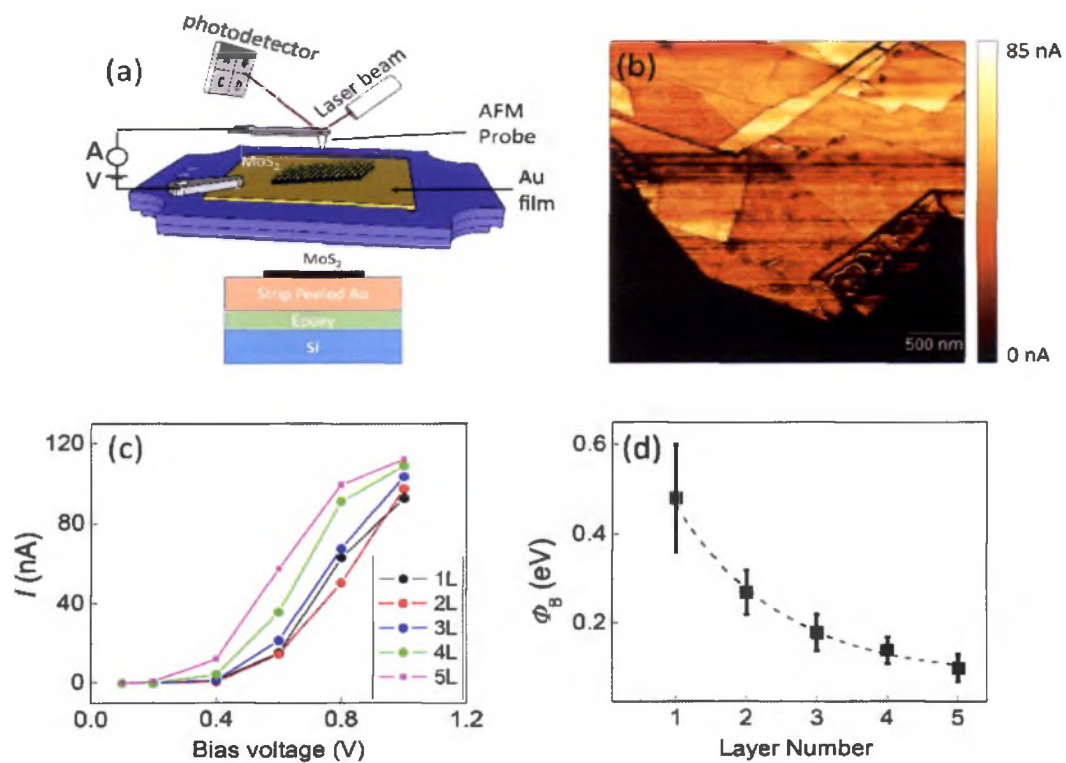


Figure 3.2 - Layer dependent conductive AFM measurement of MoS<sub>2</sub> sample on a template-stripped Au substrate. (a) (Top) Schematic diagram of the experimental setup (not to scale) used in CAFM measurements. The current is measured by a current-amplifier. (a) (Bottom) Schematic diagram of the sample (see text for details). The MoS<sub>2</sub> sample was directly exfoliated on a template-stripped Au substrate. (b) The conductive AFM data for the sample, whose height profile is shown in Fig.1 (b). (c) Current-voltage ( $I$ - $V$ ) curves for different layers obtained by averaging the current for a flake. (d) The value of the barrier height measured by taking the average of every pixel. The red line is a guide to the eye. The error bar presents the standard deviation of the barrier heights.

Since the  $I$ - $V$  curves exhibit non-linear behavior, we used Fowler-Nordheim (FN) tunneling theory to understand the layer-dependent electronic transport behavior. FN theory has been widely used to explain the tunneling of an electron between

two metals separated by an insulator or semiconductor [47-50]. The tunneling current through a thin semiconductor is given by

$$I(V) = \frac{A_e q^3 m V^2}{8\pi h \Phi_B d^2 m^*} \exp\left(-\frac{8\pi\sqrt{2m^*}\Phi_B^{3/2}d}{3hqV}\right) \quad (3.1)$$

where  $A_e$  is the effective contact area,  $h$  is Planck's constant,  $q$  is the electron charge,  $d$  is the thickness of the barrier,  $\Phi_B$  is the barrier height,  $m$  is the electron mass, and  $m^*$  is the electron effective mass inside the semiconductor. We used  $\frac{m^*}{m} \sim 0.35$  and  $0.53$  for monolayer MoS<sub>2</sub> and bulk MoS<sub>2</sub> (>1L), respectively [47]. If the layer thickness  $d$  is known, we can apply Eq. (3.1) to determine the barrier height from the  $I$ - $V$  curves. Since the conducting substrate has surface roughness much smaller ( $\sim 0.2$  nm) than the thickness of monolayer MoS<sub>2</sub> ( $\sim 0.7$  nm), the separation between the bottom conducting surface and AFM tip remain constant for a specific layer number.

By using a multiple of 1L-MoS<sub>2</sub> ( $\sim 0.7$  nm) as the layer thickness, the barrier heights for different numbers of layers were calculated as shown in Fig.3.2(d). Interestingly, we observed that the barrier height decreases as the layer number increases. This suggests that the current increases as the number of layer increases, which is clearly evident both in the current map in Fig.3.2(b) and the  $I$ - $V$  curves in Fig.3.2(c). Our observations contrast with the findings of Son *et. al.*[47],

who reported that the barrier height increases as the number of MoS<sub>2</sub> layers increase for a sample immobilized on a rough ITO surface.

### 3.3 Barrier height dependence on substrates

To understand the impact of the substrate on the barrier heights, we also studied MoS<sub>2</sub> samples on ultra-flat ITO coated single crystal quartz substrate. We found that commercially available ITO coated substrate has a high surface roughness and is not suitable for SPM measurement (see supplementary Figure A1 for details). The indium tin oxide (ITO) thin films were deposited by physical vapor deposition onto transparent Z-cut quartz substrates (see Methods for details). An AFM surface profile image of the substrate is shown in the right inset to Fig.3.1(c). The surface RMS roughness of this transparent ITO coated sample is ~ 0.7 nm.

The height profile of one MoS<sub>2</sub> sample on ITO substrate is shown in Fig.3.3(a). The current map for 1L-5L MoS<sub>2</sub> at 1.5 V bias voltage is shown in Fig.3.3(b) and clearly shows that the current increases with increasing layer number. The corresponding *I-V* curves are shown in Fig.3.3(c), which demonstrate that the current level increases, though not prominently compared to MoS<sub>2</sub> on TS-Au, as the layer number increases from 1L to 5L. Note that the current level decreases above five layers. One possible explanation to account for this observation is that the barrier height does not change significantly after the MoS<sub>2</sub> layer number exceeds five, whereas, the sample thickness increases linearly. Hence the

tunneling current decreases significantly as the sample thickness ( $d$ ) increases as predicted by the FN-Tunneling model. Further study is necessary to understand the details of the electrical transport properties of MoS<sub>2</sub> samples thicker than 5 layers. Fowler-Nordheim tunneling theory was used to calculate the barrier heights as shown in Fig.3.3(d). Although, the layer number dependence of the barrier height for MoS<sub>2</sub> on ITO is very similar to the samples immobilized on a TS-Au substrate, the barrier heights on the ITO substrate are larger than those on the TS-Au substrate, which is likely caused by different work function of ITO and Au in the presence of multilayer MoS<sub>2</sub>.

Another important feature observed in these MoS<sub>2</sub> samples (both on TS-Au and ITO substrate) is that the edges are less conducting compared to the middle of the basal plane. The current drops by 2-5 times as the tip approaches the edge compared to regions far from the edges. The low current edges are especially visible, both in Fig.3.2(b) and Fig.3.3(b), as dark lines that trace the boundaries between adjacent layers. The current profile along three different edges are presented in the supplement Fig. A2. Our estimate of the width of that insulating edge is ~20 nm, which is comparable to the Pt/Si tip width. This suggests that the insulating region is smaller than the Pt/Si tip size and is beyond our measurement capabilities with our current AFM probe and setup.

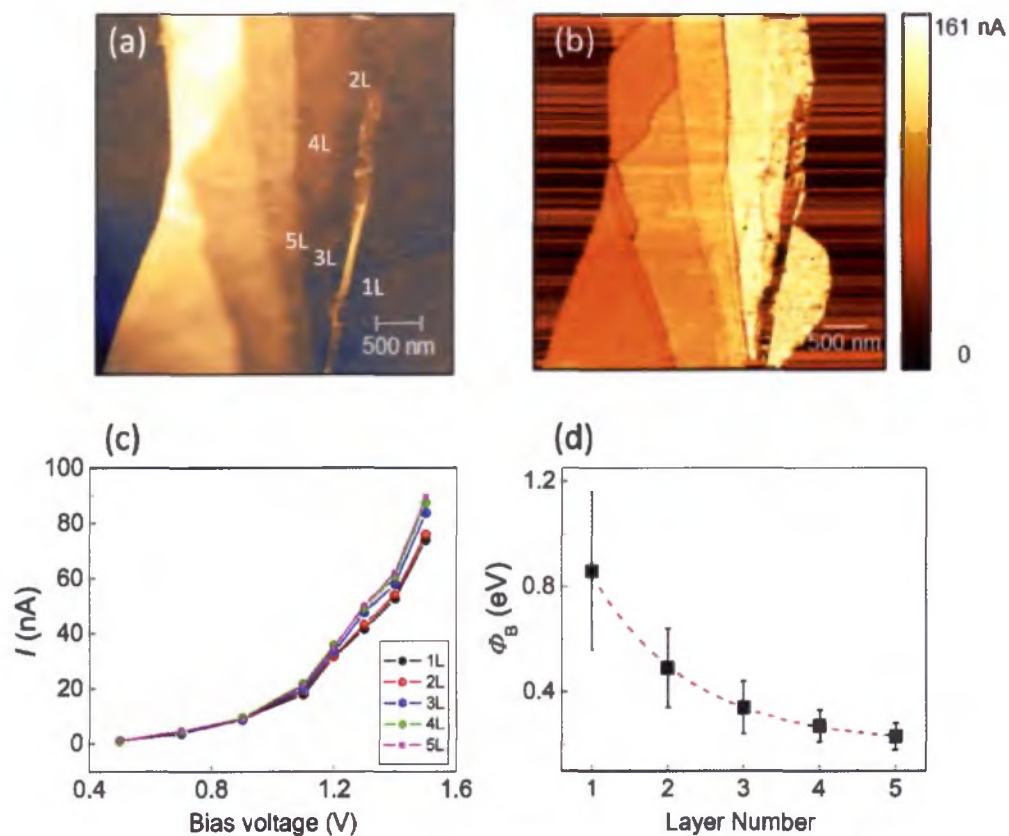


Figure 3.3 - Layer dependent conductive AFM measurement of MoS<sub>2</sub> sample on a physical vapor deposited ITO film. (a) Contact mode AFM image of the height profile of a sample on ITO coated wafer. The layer numbers are shown. The scale bar is 500 nm. (b) The conductive AFM data for the sample for 1.5 V. (c) I-V curves for different layers obtained by averaging the current. (d) Calculated average value of the barrier height measured by taking the average of every pixel. The red line is a guide to the eye. The error bar presents the standard deviation of the barrier heights.

### 3.4 Density functional theory (DFT)

To explain our experimental results, density functional theory (DFT) calculations (done by our collaborator in School of Chemical, Biological and Materials Engineering, University of Oklahoma) were performed to explore the interfacial electronic structure of 1L-5L MoS<sub>2</sub> on an Au(111) surface (Fig.3.4A). Figure 3.4B depicts the calculated electron affinity ( $\chi_e$ ) of isolated MoS<sub>2</sub> layers, which shows an incremental increase of the electron affinity (lower conduction band minimum) with increased layer number. The electron affinity reaches a plateau at about 4 layers. Figure 3.4C shows the calculated Schottky barrier, which has been calculated as  $\phi_B = W - \chi_e$ , where  $W$  is the work function of gold. The calculated work function is shown in Figure A3 and shows a systematic decrease with layer thickness for the optimized structures. Fig.3.4C also shows the effect of increasing the interfacial distance between the MoS<sub>2</sub> layers and the substrate. The imposed interfacial separation accounts for the possibility that the experimental interfacial spacing may not be exactly the same as the DFT-optimized ones (black curve in Fig.3.4C) due to the corrugation of the Au surface as well as contaminants at the interface. The calculated Schottky barriers for an interlayer spacing of 1-3 Å between Au and MoS<sub>2</sub> shows the general trend of decreasing barrier with increasing layer number. In all cases with an imposed interlayer spacing,  $\phi_B$  reaches a plateau after 3 layers, which is more or less line with the experimental results.

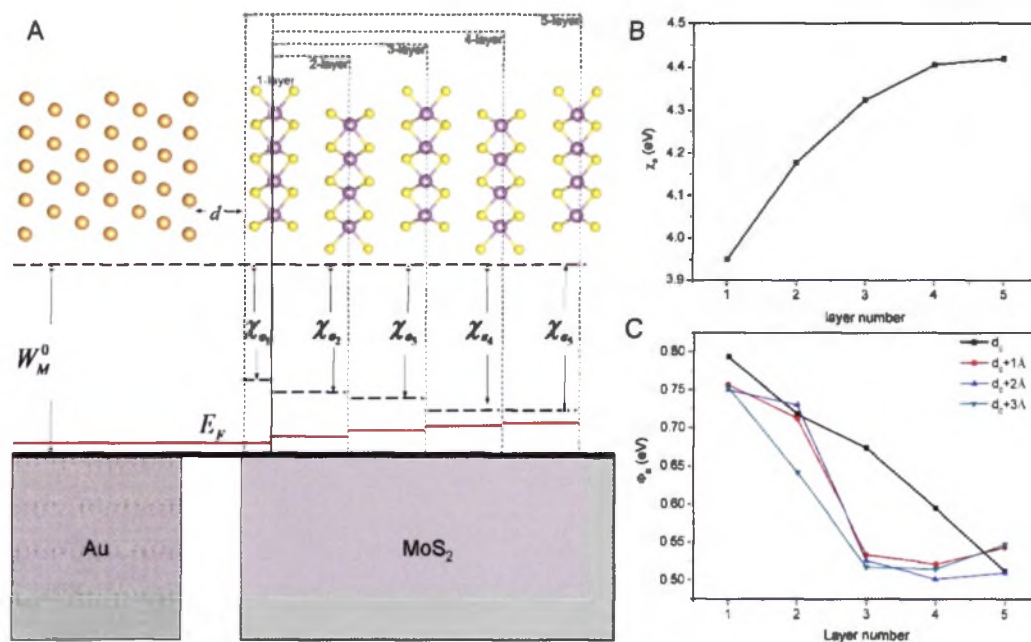


Figure 3.4 - DFT calculated interfacial electronic structure of the Au/MoS<sub>2</sub>. (A) Schematic of the MoS<sub>2</sub>/Au interface and band alignment. (B) DFT-calculated electron affinity of MoS<sub>2</sub> with different thickness. (C) DFT-calculated Schottky barrier at the interface of MoS<sub>2</sub>/Au with varying thickness of MoS<sub>2</sub> and interfacial spacing. The black curve shows the values from DFT-optimized structures, while the red, blue and green ones show the values when the structures are artificially displaced by 1, 2 and 3 Å further way from the Au surface, respectively.

The DFT calculations were performed within the framework of plane-wave method as implemented in the VASP code [51]. The exchange and correlation potential was described by using the generalized gradient approximation (GGA) in the scheme of Perdew-Burke-Ernzerhof (PBE) functional [52] and the projector-augmented wave method [53, 54] was employed to give the numerical description of the ion-electron interaction. A cutoff energy of 400 eV was used to limit the plane-wave basis set. The equilibrium distances between the optimized Au

substrate and MoS<sub>2</sub> with different layer numbers were determined by calculating the minima of the energy versus distance curves as relaxed under the stop criterion of 0.03 eV/Å per atom. A vacuum layer of 40 Å has been added to each composite structure of Au and MoS<sub>2</sub> to simulate the surface configuration. The Van der Waals (vdW) correction based on the Grimme's DFT-D2 method [55] and dipole correction along the direction vertical to the interface have been included to calculate the total energies and electrostatic potentials, which can provide the reasonable atomic configurations at the interfaces and the vacuum potentials.

## Chapter 4

### Optical properties of MoS<sub>2</sub>

We now discuss the optoelectronic behavior of exfoliated 1L-5L MoS<sub>2</sub> sample on an ultra-flat ITO substrate. The MoS<sub>2</sub> (1L-5L) samples were immobilized on a transparent ITO substrate. The AFM stage was mounted on an inverted Zeiss microscope. The MoS<sub>2</sub> was illuminated through the quartz substrate with an LED source (X-Cite® 110), which employed a dichroic filter to select the excitation wavelength range of 460-490 nm (Fig 4.1). The excitation light was guided by a microscope objective (x20, NA~0.75) to the sample. The beam area was ~10 μm with optical power density  $P \sim 4 \text{ mW}/\mu\text{m}^2$ .

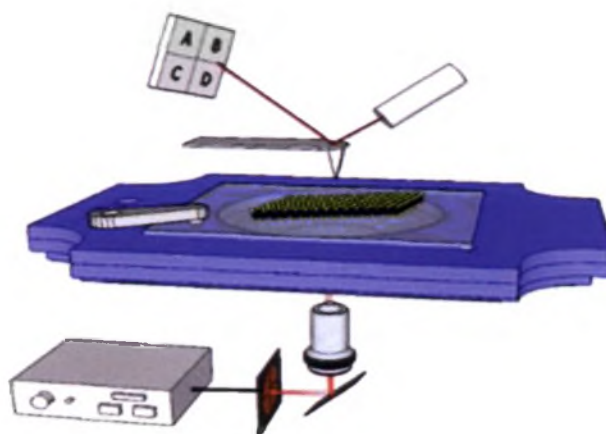


Figure 4.1 – An external light source (460-490 nm) provides illumination to the MoS<sub>2</sub> sample from the bottom of the C-AFM stage. The light is focused on the sample through a 20x lens.

#### 4.1 Negative conductance under illumination

The height profile of the sample is shown in Fig. 4.2(a) where different layer regions are marked. The corresponding  $I$ - $V$  curve for 1L-MoS<sub>2</sub> is shown in Fig. 4.2(b). Surprisingly, the current decreases as the sample is illuminated by 460-490 nm photons demonstrating negative photoconductivity. Note that the change in photocurrent ( $\Delta I_{PC}$ ) become larger as we increase the bias voltage. The difference in current under illumination  $\Delta I_{PC}(= I_{light} - I_{dark})$  for  $V_{ds} = 1$  V is shown as a spatial map in Fig. 4.2(c). The spatial map was made by subtracting the AFM current image acquired illuminated with blue light from the one without illumination. The spatial map clearly shows that the current decreased under illumination. Another interesting feature is that  $\Delta I_{PC}$  becomes more negative as the layer number increases. The observation of negative photoconductivity of single crystal MoS<sub>2</sub> nano-sheet is an anomalous photoresponse compared to regular positive photoconductivity behavior observed for planar structured TMDs [4, 6, 12, 13].

Negative photoconductivity of MoS<sub>2</sub> nano-sheet (Fig 4.3) connected by two metal electrodes in a planar or horizontal configuration was observed previously and the effect was attributed to the strong many-body interactions in MoS<sub>2</sub> [56, 57]. This many-body related negative photoconductivity in planar MoS<sub>2</sub> device configuration has transient nature with lifetimes on the order of trions (~picoseconds). On the other hand, negative photoconductivity observed in our vertical

metal/semiconductor/metal device structure is non-transient or time-independent, which suggests that the origin of negative photoconductivity in our devices is completely different than that in planar device configurations. One possible explanation is that the excited electrons and holes after optical illumination in MoS<sub>2</sub> modify the barrier height, which therefore changes the tunneling current. Strong negative photoconductivity measured across the basal plane suggests that the barrier height increases due to optical illumination, which in turn reduces the tunneling current. Because photoconductivity is a critical parameter applied to optoelectronics, further study is necessary to elucidate the origin of this DC negative photoconductivity.

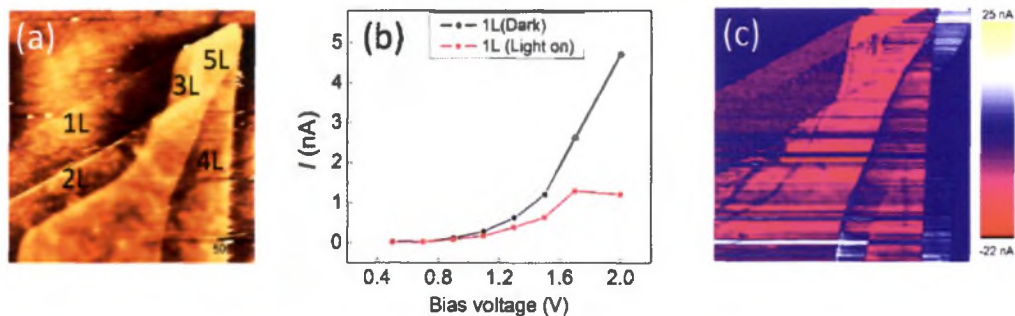


Figure 4.2 - Photoconductive AFM measurement of sample on an ultra-flat ITO coated single crystal quartz. (a) Contact mode AFM image of the height profile of the sample. The monolayer region is marked. (b) The IV curve when the sample is illuminated by blue light (black circle) and in the dark (red circle). (c) The photoconductive AFM image of the sample at bias voltage of 1 V. The image is obtained by subtracting the illuminated photoconductive AFM image from the conductive AFM image measured in the dark.

## 4.2 Photocurrent measurements using a lock-in amplifier

The optoelectronic behavior was further examined using a different MoS<sub>2</sub> sample on ITO (Fig 4.4). A blue laser (wavelength 480 nm) was used as the excitation source. In addition, we connected the lock-in system externally to the AFM electrical output channels. The laser that shines on the sample was modulated with a high-frequency pulse (~9.8 kHz) generated by the lock-in system as shown in Fig 4.3. Since the photocurrent (AC current) from the sample oscillates in sync with this modulation frequency, lockin measures the current only due to laser excitation and eliminates the DC current due to the bias voltage.

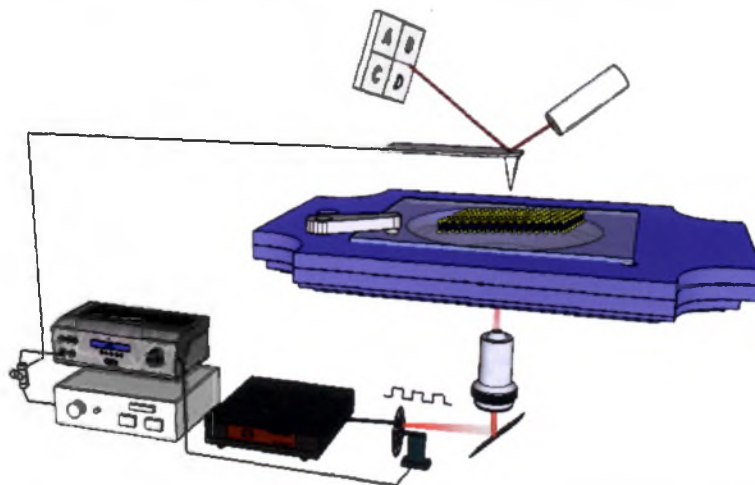


Figure 4.3 – A schematic drawing of the photocurrent measurements setup. The photocurrent (AC) is measured by using the lock-in amplifier which modulates the laser with a high frequency (~9.8 kHz). The output of the AFM signal is split into two channels, one goes to the lock-in system for photocurrent extraction and one goes to the regular DC current channel.

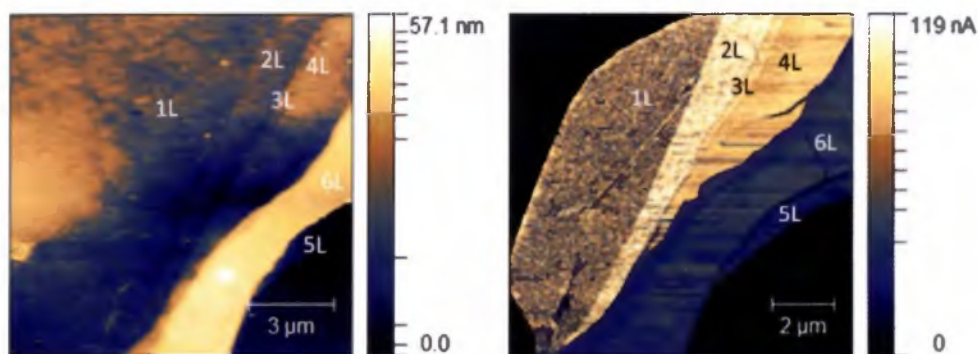


Figure 4.4 – The sample MoS<sub>2</sub> nano-sheet sample used for photocurrent study. Left: the height measurement of the sample showing the multi-layers feature. The layer thickness increases from the left to the right across the image. Right: The current measured in the dark showing a distinct current pattern on different layers as seen from the previous sample.

The lock-in photocurrent measurements were conducted in three different ways (i) sample was illuminated with a laser under a constant intensity while varying the applied voltage; (ii) a constant voltage was applied to the sample while varying the laser intensity; (iii) zero applied voltage was applied to the sample and the laser intensity is kept at a constant. There are a few features we observed from these measurements. Each will be discussed in the following sections.

### 4.3 Dependence of photocurrent on layer number

Fig 4.5 shows the photocurrent response of the MoS<sub>2</sub> nano-sheet under illumination. The distribution of the current on each layer is different from the DC current (Fig 4.4 - right). Fig 4.6 presents the photocurrent magnitudes measured with the laser power intensity fixed at its maximum ( $6.8 \text{ mW}/\mu\text{m}^2$ ) while the voltage increasing from 0.2 V to 1.2 V with an increment of 0.2 V. A typical tunneling  $I$ - $V$  behavior was observed in the photocurrent of monolayers and bilayers. For layers

thicker than bi-layer the photocurrent seems insensitive to the applied voltage. This could be due to the excitons generated in the first few layers near the substrate having much less tunneling probability as the layer thickness increases.

One other distinct feature that is different from the DC current (Fig 4.4 - right) is the photo active boundaries existing between the MoS<sub>2</sub> layers. In DC current, MoS<sub>2</sub> nano-sheet shows insulating edges behavior in which the current drops significantly across the layers. In AC photocurrent measurements, the edges of the MoS<sub>2</sub> layers exhibit a larger amount of currents. Further study is necessary to understand the photocurrent behavior of the edges.

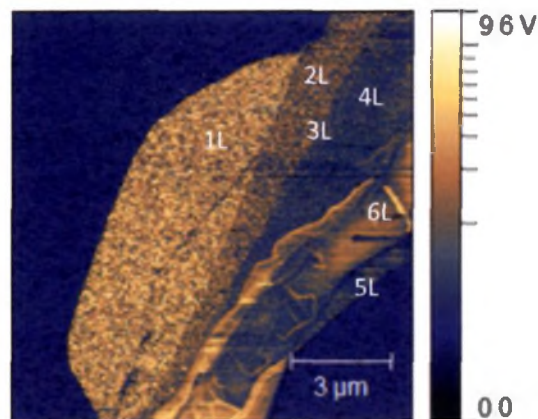


Figure 4.5 – A C-AFM current image. Photocurrent response of MoS<sub>2</sub> showing a different current distribution pattern on the layers and photo active edges. The insulating edges observed in the DC current image are not seen in this photocurrent image.

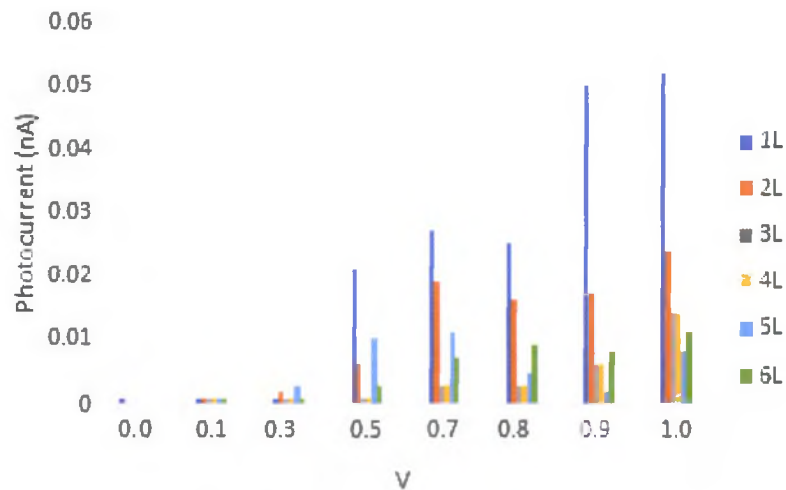


Figure 4.6 – The photocurrent (AC) of MoS<sub>2</sub> measured with voltage going from 0V to 1V while keeping the laser intensity constant (maximum power). Photocurrent on mono and bi-layers shows a strong photoresponse and is relatively more dependent on the applied voltage. Layers thicker than bi-layer (>2L) have less photocurrent and are less dependent on the applied voltage.

In Fig 4.7 the current distribution within the layers basically stays the same, however, the current level fluctuates on some of the layers as the light intensity goes up. We suspected that this current fluctuation comes from the negative potential caused by the photovoltaic effect across the depletion region. As the power intensity increases, the combined effects of increasing free charge carriers and the negative potential have to be taken in to account for getting the total photocurrent. The middle layers are again less responsive to the changing laser power intensity.

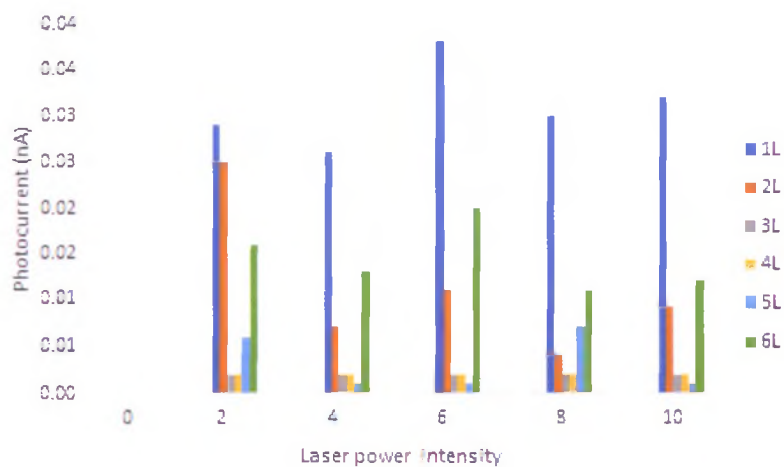


Figure 4.7 – The photocurrent (AC) of MoS<sub>2</sub> measured with increasing laser intensity while keeping the applied voltage constant. The drop of the current on some of the layers under a higher light intensity could be due to the negative potential caused by the photovoltaic effect.

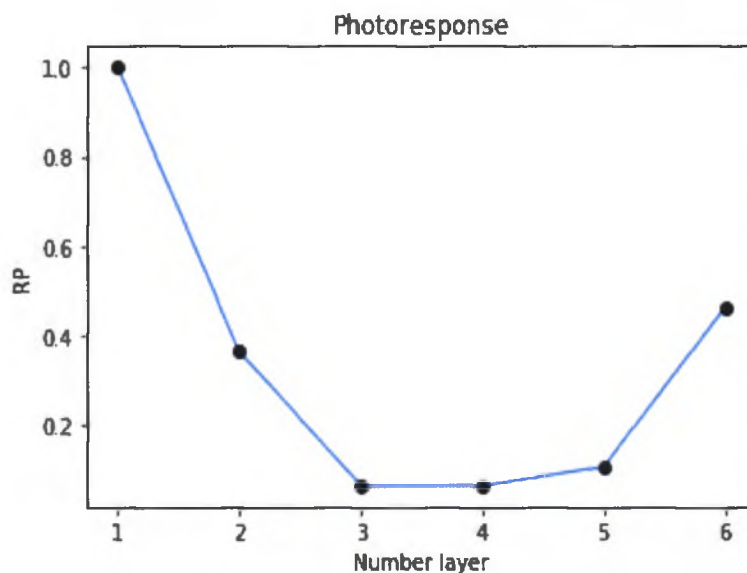


Figure 4.8 – Normalized photoresponse (PR) for the first few layers of MoS<sub>2</sub>. The monolayer has the dominant PR due to its direct bandgap nature. The PR reaches its minimum at around the tri-layer then bounces back gradually due to higher light absorption of the light in the thicker layers. This layer dependent behavior is very similar to the results obtained by Son *et al* [47].

By taking an average and normalizing the photoresponse at each power intensity in Fig 4.7, we obtained the photoresponse (PR) in relation to the number of layers (Fig 4.8).

The significant photoresponse in monolayer MoS<sub>2</sub> is due to its direct band-gap nature which allows the electrons in the valence band to be excited to the conduction band by absorbing the incoming photons. The photoresponse drops quickly with the next few layers due to the direct-to-indirect band-gap transition. The photoresponse reaches the minimum at around the tri-layer region and then starts to increase gradually as the layer number continues to increase. This gradual restoration of the photoresponse is attributed to the increased absorption of light through the thicker layers.

#### 4.4 Photothermoelectric effect (PTE)

Lastly, CAFM measurements were performed with zero applied voltage and the laser intensity is kept at some constant. Interestingly, some small current signals were still detected in the output channels (Fig 4.9). This small current is attributed to the photothermoelectric effect (PTE). When the light is shining onto the sample, absorption of the photoenergy in the sample converts into heat and rises the temperature. The temperature difference between of the sample and substrate creates a potential across the junction and thus creates a current. This PTE current is about a few hundreds of pico-Amp.

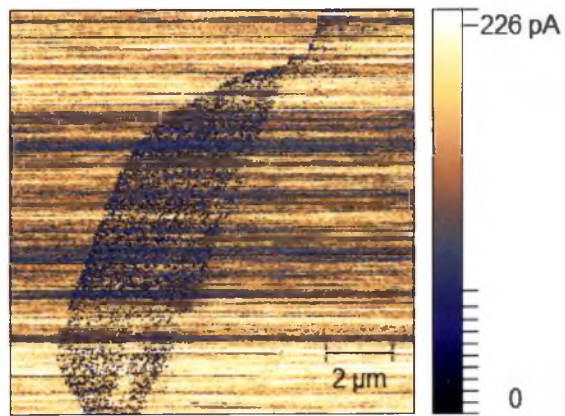


Figure 4.9 –The PTE was seen when the sample was applied with zero voltage and was illuminated with a blue laser of 480 nm wavelength at  $6.8 \text{ mW}/\mu\text{m}^2$  intensity.

## Chapter 5

### Conclusion

In conclusion, electrical and optoelectronic properties of 1L-5L MoS<sub>2</sub> samples residing on two different atomically flat conducting surfaces are probed by using CAFM and PCAFM measurements. We have observed five important features of electrical and optoelectronic properties. First, fitting our data to the Fowler-Nordheim tunneling theory reveals that the barrier heights are dependent on the number of layers; barrier heights is the highest for monolayer and then monotonically decreases as the layer number increases. By using DFT calculation, we attributed this to the increase electron affinity as the layer number increases. Second, the barrier height for a specific MoS<sub>2</sub> layer sample depends on the type of the conducting substrate underneath the sample. Third, the edges of MoS<sub>2</sub> are less conducting. Fourth, negative DC photoconductivity is observed by illuminating the sample with a blue light ( $\lambda \sim 460-490$  nm). Fifth, the photocurrent (AC) of the MoS<sub>2</sub> illuminated with a laser of wavelength 480 nm shows a strong dependence on layer number and applied voltage. Monolayer has the highest photoresponse due to its direct band-gap nature. On the contrary, the middle layer (>2L) is much less responsive to the illumination resulting in a smaller photocurrent.

Photocurrent from our samples shows a different response with the DC current. Both currents show a strong dependence on the number layer and the applied

voltage. The photoresponse extracted from our data roughly matches the model prediction [47], however, there was a difficulty in obtaining consistent barrier height of the MoS<sub>2</sub>/ITO junction under illumination using the equations in Fowler Nordheim theory. Moreover, the magnitude of the photocurrent measured using the lock-in amplifier is on the order of less than 1 nA which is much less than the current drop measured in the DC bias with illumination. Therefore further study is needed in order to fully understand the optical behaviors of the Metal/MoS<sub>2</sub> junction.

Our study revealed the complex interfacial electrical and optoelectronic properties of MoS<sub>2</sub> when in contact with an atomically flat metal. These Metal/TMDs interfaces may lead to the development of nanoscale optoelectronic devices with tailored properties.

## Appendix

### A1. TE-Au surface roughness

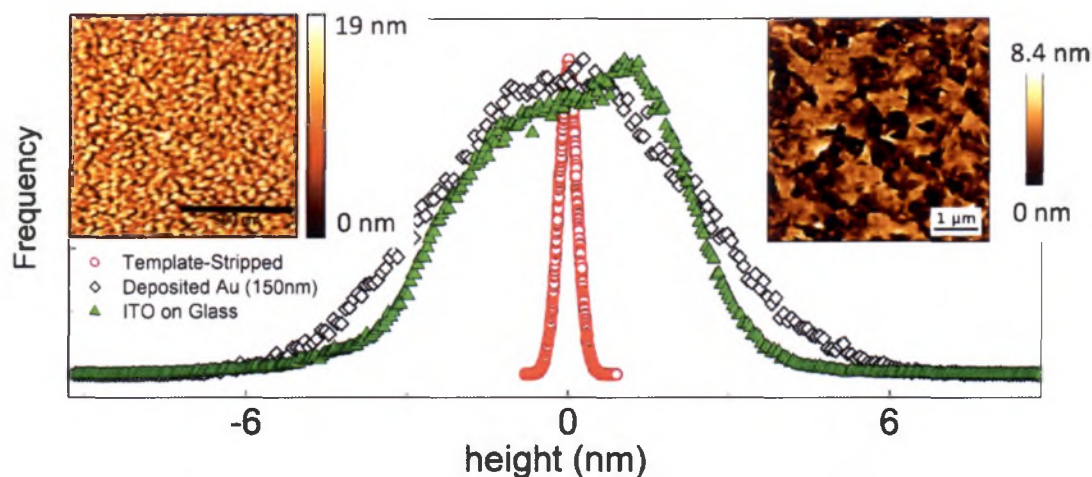


Figure A1: Surface roughness of thermally evaporated Au substrate and commercially available ITO on glass substrate (Delta Technologies). Main panel: histogram of the height distribution (surface roughness measured by AFM) of the template-stripped Au substrate (red circle), as thermally evaporated Au (black square) substrate of thickness  $\sim 150$  nm and commercial ITO on glass substrate (green triangle). The root mean squared (RMS) value of the surface roughness measured was  $\sim 0.18$  nm for template-stripped Au and  $\sim 1.8$  nm for as deposited Au substrate and  $\sim 1.9$  nm for ITO on glass substrate. Inset-left: tapping mode AFM image of the thermally evaporated Au surface. Inset-right: tapping mode AFM image ITO coated glass substrate. A Gaussian fit to the height data provides full width at half maxima (FWHM)  $\sim 0.3$  nm for the template-stripped Au,  $\sim 5$  nm for as deposited Au and  $\sim 4$  nm for the ITO substrate.

## A2. Electronic transport along the edges

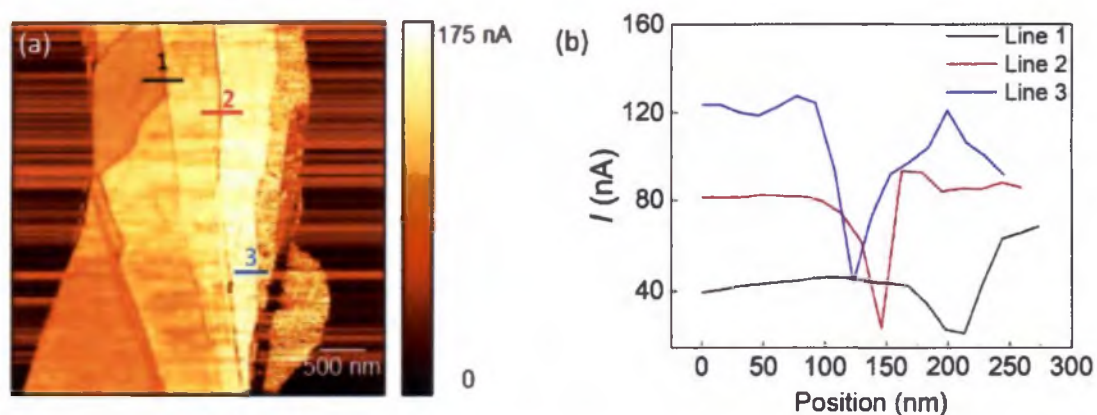


Figure A2: Fig. (a) is presenting the current map of MoS<sub>2</sub> sample on an ITO substrate. The current is measured at 1.3 V. Three lines of different (black, red and blue) are marked whose current profiles are presented in Fig. (b).

## A3. Work function calculations

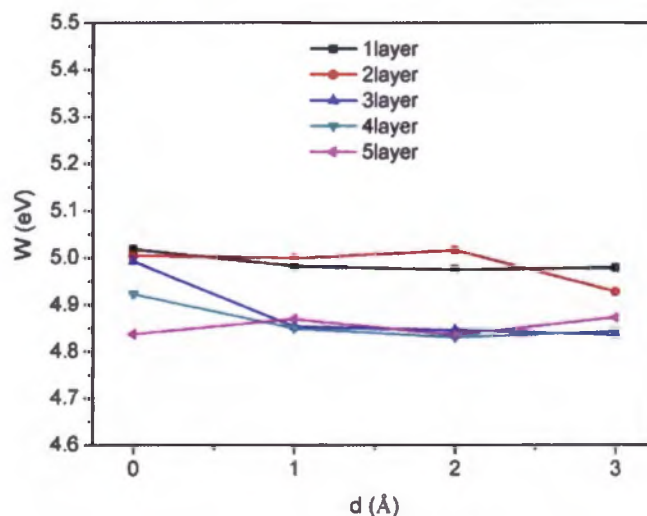


Figure A3: Calculated work function of MoS<sub>2</sub> on Au as a function of the thickness of MoS<sub>2</sub> and the interfacial spacing between the first layer of MoS<sub>2</sub> and the Au (111) surface. This work function has been used to calculate the Schottky barrier in Figure 4.4C in the main text.

## References

1. Mak, K.F., et al., *Atomically Thin MoS<sub>2</sub>: A New Direct-Gap Semiconductor*. Physical Review Letters, 2010. **105**(13): p. 136805.
2. Xiao, D., et al., *Coupled Spin and Valley Physics in Monolayers of MoS<sub>2</sub> and Other Group-VI Dichalcogenides*. Physical Review Letters, 2012. **108**(19): p. 196802.
3. Wang, Q.H., et al., *Electronics and optoelectronics of two-dimensional transition metal dichalcogenides*. Nat Nano, 2012. **7**(11): p. 699-712.
4. Mak, K.F. and J. Shan, *Photonics and optoelectronics of 2D semiconductor transition metal dichalcogenides*. Nat Photon, 2016. **10**(4): p. 216-226.
5. Xia, F., et al., *Two-dimensional material nanophotonics*. Nat Photon, 2014. **8**(12): p. 899-907.
6. Duan, X., et al., *Two-dimensional transition metal dichalcogenides as atomically thin semiconductors: opportunities and challenges*. Chemical Society Reviews, 2015. **44**(24): p. 8859-8876.
7. Jariwala, D., et al., *Emerging Device Applications for Semiconducting Two-Dimensional Transition Metal Dichalcogenides*. ACS Nano, 2014. **8**(2): p. 1102-1120.
8. Manzeli, S., et al., *2D transition metal dichalcogenides*. Nature Reviews Materials, 2017. **2**: p. 17033.
9. Splendiani, A., et al., *Emerging Photoluminescence in Monolayer MoS<sub>2</sub>*. Nano Letters, 2010. **10**(4): p. 1271-1275.
10. Howell, S.L., et al., *Investigation of Band-Offsets at Monolayer–Multilayer MoS<sub>2</sub> Junctions by Scanning Photocurrent Microscopy*. Nano Letters, 2015. **15**(4): p. 2278-2284.
11. Britnell, L., et al., *Strong Light-Matter Interactions in Heterostructures of Atomically Thin Films*. Science, 2013. **340**(6138): p. 1311-1314.
12. Klots, A.R., et al., *Probing excitonic states in suspended two-dimensional semiconductors by photocurrent spectroscopy*. Sci. Rep., 2014. **4**: p. 6608.
13. Lopez-Sanchez, O., et al., *Ultrasensitive photodetectors based on monolayer MoS<sub>2</sub>*. Nature Nanotechnology, 2013. **8**(7): p. 497-501.
14. Baugher, B.W.H., et al., *Optoelectronic devices based on electrically tunable p-n diodes in a monolayer dichalcogenide*. Nat Nano, 2014. **9**(4): p. 262-267.
15. Eda, G. and S.A. Maier, *Two-Dimensional Crystals: Managing Light for Optoelectronics*. ACS Nano, 2013. **7**(7): p. 5660-5665.
16. Ross, J.S., et al., *Electrically tunable excitonic light-emitting diodes based on monolayer WSe<sub>2</sub> p-n junctions*. Nat Nano, 2014. **9**(4): p. 268-272.
17. Sundaram, R.S., et al., *Electroluminescence in Single Layer MoS<sub>2</sub>*. Nano Letters, 2013. **13**(4): p. 1416-1421.

18. Tsai, D.-S., et al., *Few-Layer MoS<sub>2</sub> with High Broadband Photogain and Fast Optical Switching for Use in Harsh Environments*. ACS Nano, 2013. 7(5): p. 3905-3911.
19. Wu, C.-C., et al., *Elucidating the Photoresponse of Ultrathin MoS<sub>2</sub> Field-Effect Transistors by Scanning Photocurrent Microscopy*. J. Phys. Chem. Lett., 2013. 4(15): p. 2508-2513.
20. Yin, Z., et al., *Single-Layer MoS<sub>2</sub> Phototransistors*. ACS Nano, 2011. 6(1): p. 74-80.
21. Tsai, M.-L., et al., *Monolayer MoS<sub>2</sub> Heterojunction Solar Cells*. ACS Nano, 2014. 8(8): p. 8317-8322.
22. Bernardi, M., M. Palummo, and J.C. Grossman, *Extraordinary Sunlight Absorption and One Nanometer Thick Photovoltaics Using Two-Dimensional Monolayer Materials*. Nano Letters, 2013. 13(8): p. 3664-3670.
23. Peng, B., P.K. Ang, and K.P. Loh, *Two-dimensional dichalcogenides for light-harvesting applications*. Nano Today, 2015. 10(2): p. 128-137.
24. Tonndorf, P., et al., *Single-photon emission from localized excitons in an atomically thin semiconductor*. Optica, 2015. 2(4): p. 347-352.
25. Chakraborty, C., et al., *Voltage-controlled quantum light from an atomically thin semiconductor*. Nat Nano, 2015. 10(6): p. 507-511.
26. He, Y.-M., et al., *Single quantum emitters in monolayer semiconductors*. Nat Nano, 2015. 10(6): p. 497-502.
27. Srivastava, A., et al., *Optically active quantum dots in monolayer WSe<sub>2</sub>*. Nat Nano, 2015. 10(6): p. 491-496.
28. Koperski, M., et al., *Single photon emitters in exfoliated WSe<sub>2</sub> structures*. Nat Nano, 2015. 10(6): p. 503-506.
29. Wu, S., et al., *Monolayer semiconductor nanocavity lasers with ultralow thresholds*. Nature, 2015. 520: p. 69.
30. Cao, T., et al., *Valley-selective circular dichroism of monolayer molybdenum disulphide*. Vol. 3. 2012. 887.
31. Zeng, S., et al., *Graphene-MoS<sub>2</sub> Hybrid Nanostructures enhanced Surface Plasmon Resonance Biosensors*. Vol. 207. 2015. 801-810.
32. Li, T. and G. Galli, *Electronic Properties of MoS<sub>2</sub> Nanoparticles*. The Journal of Physical Chemistry C, 2007. 111(44): p. 16192-16196.
33. Kufer, D. and G. Konstantatos, *Highly Sensitive, Encapsulated MoS<sub>2</sub> Photodetector with Gate Controllable Gain and Speed*. Nano Letters, 2015. 15(11): p. 7307-7313.
34. Lee, H.S., et al., *Metal Semiconductor Field-Effect Transistor with MoS<sub>2</sub>/Conducting NiOx van der Waals Schottky Interface for Intrinsic High Mobility and Photo-Switching Speed*. Vol. 9. 2015.
35. Sze, S.M. and K. K. Ng, *Physics of Semiconductor Devices / S.M. Sze, K.K. NG* 2019.

36. Svensson, J. and E. Campbell, *Schottky barriers in carbon nanotube-metal contacts*. Vol. 110. 2011. 111101-111101.
37. Gu, Q., et al., *Hydrogen peroxide treatment induced rectifying behavior of Au/n-ZnO contact*. Vol. 90. 2007. 122101-122101.
38. Li, Y., C.-Y. Xu, and L. Zhen, *Surface potential and interlayer screening effects of few-layer MoS<sub>2</sub> nanoflakes*. Vol. 102. 2013.
39. Novoselov, K.S., et al., *Electric Field Effect in Atomically Thin Carbon Films*. Vol. 306. 2004. 666-9.
40. Nečas, D. and P. Klapetek, *Gwyddion: An open-source software for SPM data analysis*. Vol. 10. 2011.
41. Chakraborty, B., et al., *Layer-dependent resonant Raman scattering of a few layer MoS<sub>2</sub>*. Vol. 44. 2013. 92-96.
42. Hegner, M., P. Wagner, and G. Semenza, *Ultralarge atomically flat template-stripped Au surfaces for scanning probe microscopy*. *Surface Science*, 1993. **291**(1): p. 39-46.
43. Blackstock, J.J., et al., *Ultra-flat platinum surfaces from template-stripping of sputter deposited films*. *Surface Science*, 2003. **546**(2): p. 87-96.
44. Ragan, R., et al., *Atomic Surface Structure of UHV-Prepared Template-Stripped Platinum and Single-Crystal Platinum(111)*. *The Journal of Physical Chemistry B*, 2004. **108**(52): p. 20187-20192.
45. Lee, S., et al., *Scanning Tunneling Microscopy of Template-Stripped Au Surfaces and Highly Ordered Self-Assembled Monolayers*. *Langmuir*, 2008. **24**(12): p. 5984-5987.
46. Dean, C.R., et al., *Boron nitride substrates for high-quality graphene electronics*. *Nat Nano*, 2010. **5**(10): p. 722-726.
47. Son, Y., et al., *Layer Number Dependence of MoS<sub>2</sub> Photoconductivity Using Photocurrent Spectral Atomic Force Microscopic Imaging*. *ACS Nano*, 2015. **9**(3): p. 2843-2855.
48. Ahmed, F., et al., *Carrier transport at the metal–MoS<sub>2</sub> interface*. *Nanoscale*, 2015. **7**(20): p. 9222-9228.
49. Hattori, Y., et al., *Determination of Carrier Polarity in Fowler–Nordheim Tunneling and Evidence of Fermi Level Pinning at the Hexagonal Boron Nitride/Metal Interface*. *ACS Applied Materials & Interfaces*, 2018. **10**(14): p. 11732-11738.
50. Lee, S., et al., *Tunneling transport of mono- and few-layers magnetic van der Waals MnPS<sub>3</sub>*. *Apl Materials*, 2016. **4**(8).
51. Kresse, G. and J. Furthmüller, *Efficient iterative schemes for ab initio total-energy calculations using a plane-wave basis set*. *Physical Review B*, 1996. **54**(16): p. 11169-11186.
52. Perdew, J.P., K. Burke, and M. Ernzerhof, *Generalized Gradient Approximation Made Simple*. *Physical Review Letters*, 1996. **77**(18): p. 3865-3868.

53. Blöchl, P.E., *Projector augmented-wave method*. Physical Review B, 1994. **50**(24): p. 17953-17979.
54. Kresse, G. and D. Joubert, *From ultrasoft pseudopotentials to the projector augmented-wave method*. Physical Review B, 1999. **59**(3): p. 1758-1775.
55. Grimme, S., et al., *A consistent and accurate ab initio parametrization of density functional dispersion correction (DFT-D) for the 94 elements H-Pu*. The Journal of Chemical Physics, 2010. **132**(15): p. 154104.
56. Lui, C.H., et al., *Trion-Induced Negative Photoconductivity in Monolayer MoS<sub>2</sub>*. Physical Review Letters, 2014. **113**(16): p. 166801.
57. Junpeng, L., L. Hongwei, and S. Jing, *Negative terahertz photoconductivity in 2D layered materials*. Nanotechnology, 2017. **28**(46): p. 464001.